Ice Accretion Simulations on Airfoils

*Serkan Özgen *, Nermin Uğur *, İlhan Görgülü ** and Volkan Tatar ***
**Middle East Technical University, Dept. Aerospace Eng.*
Dumlupınar Bul. No:1, 06800, Çankaya, Ankara, Turkey
*** Turkish Engine Industries Inc.*
Esentepe Mah. Çevreyolu Bul. No:356, 26003 Tepebaşı, Eskişehir, Turkey

Abstract

In the current study, ice shape predictions for NACA0012 airfoil and collection efficiency predictions for Twin Otter airfoil are obtained. The results are validated with reference numerical and experimental data. Ice accretion modeling mainly consists of four steps: flow field solution, droplet trajectory calculations, thermodynamic analyses and ice accretion with Extended Messinger model. The models are implemented in a FORTRAN code to perform icing analyses for 2D geometries. The results are in good agreement with the reference data. It is deduced that increasing computational layers in calculations improves ice shape predictions. The results indicate that collection efficiencies and impingement zone increase with increasing droplet diameter.

1. Introduction

Ice accretion on airframes during flight may cause great danger due to aerodynamic performance degradation and engine power loss. Hence, it is very crucial to simulate ice accretion in order to predict ice mass that accumulates on the surface and the regions which are prone to icing. Such a simulation will be useful to design and develop a de/anti-icing system for aircrafts and for airworthiness certification purposes.

In this study, ice shape predictions for NACA0012 and collection efficiency distributions for Twin Otter airfoils are obtained. In the current approach, panel method is used for the flow field solution. Droplet trajectories, collection efficiency calculations and convective heat transfer coefficient calculations are performed with the same approach as in the study of Özgen and Canıbek [1]. The study of Myers [2] is used as a base for the ice accretion model.

This manuscript summarizes the methods which are used in the developed computational tool. The results contain ice shape predictions for varying median droplet diameters (MVD), liquid water content (LWC), temperature, velocity and exposure time. The effect of Supercooled Large Droplets (SLD) on ice shape calculation is also investigated. Collection efficiency analyses are performed for different MVD and angle of attack (α). Comparisons with numerical and experimental data available in the literature are also presented.

2. Methodology

In this section, four modules used in the current approach are explained in detail.

2.1 Flow Field Solution

2-D Hess-Smith panel method is used to determine the flow velocities required for droplet trajectory calculations. The external velocity distribution is also provided, which is used in boundary layer calculations to obtain heat transfer coefficients. In this model, the airfoil is divided into quadrilateral panels, each having a constant strength source singularity element plus a vortex singularity that is constant for all panels. Using the flow tangency boundary condition at the collocation points of the surface panels, the singularity strengths are obtained. This provides the velocity potential, in other words, the flow velocity components at any point in the flow field.

2.2 Droplet Trajectories and Collection Efficiency Calculations

The following assumptions are used for droplet trajectories:

- Droplets are assumed to be spherical.
- The flow field is not affected by the droplets.
- Gravity and aerodynamic drag are the only forces acting on the droplets.

The governing equations for droplet trajectories are:

$$m\ddot{x}_p = -D\cos\gamma \tag{1}$$

$$m\ddot{y}_p = -D\cos\gamma + mg \tag{2}$$

$$\gamma = \tan^{-1}\frac{\dot{y}_p - V_y}{\dot{x}_p - V_x}, \tag{3}$$

$$D = \frac{1}{2}\rho V_{rel}^2 C_D A_p, \tag{4}$$

$$V_{rel} = \sqrt{(\dot{x}_p - V_x)^2 + (\dot{y}_p - V_y)^2} \tag{5}$$

In the above equations, V_x and V_y are the flow velocity components at the droplet location, while $\dot{x}_p, \dot{y}_p, \ddot{x}_p$ and $\ddot{y}_p$ are the components of the droplet velocity and acceleration, respectively. Atmospheric density is denoted by ρ, while droplet cross-sectional area and drag coefficient are represented by A_p and C_D, respectively. The droplet drag coefficient is computed as a function of the droplet Reynolds number, $Re = \rho V_{rel} d_p/\mu$ based on the droplet diameter d_p, relative
droplet velocity V_{rel}, and the atmospheric viscosity μ.

Drag coefficients for droplets are calculated using an empirical drag law based on the droplet Reynolds number [3]. The droplet trajectories are obtained with the integration of equations (1) and (2) over time until the impact of the droplets to the geometry. The particle impact pattern on the section determines the amount of water that impinges on the surface and the region subject to icing. The local collection efficiency (β) is defined as the ratio, of the area of impingement to the area through which water passes at some distance upstream of the section.

2.3 Thermodynamic Analysis

In order to calculate the convective heat transfer coefficients, a 2-D Integral Boundary Layer Method is employed for both laminar and turbulent flow [1].

2.4 Extended Messinger Model

Ice accretion on the geometry is found with the Extended Messinger Method. The ice shape prediction is based on phase change or the Stefan problem. The governing equations for the phase change problem are mainly: energy equations in the ice and water layers, mass conservation equation and a phase change condition at the ice/water interface [1].

$$\frac{\partial T}{\partial t} = \frac{k_i}{\rho_i C_{pi}}\frac{\partial^2 T}{\partial y^2} \tag{6}$$

$$\frac{\partial \theta}{\partial t} = \frac{k_w}{\rho_w C_{pw}}\frac{\partial^2 \theta}{\partial y^2} \tag{7}$$

$$\rho_i \frac{\partial B}{\partial t} + \rho_w \frac{\partial h}{\partial t} = \rho_a \beta V_\infty + \dot{m}_{in} - \dot{m}_{e,s} \tag{8}$$

$$\rho_i L_F \frac{\partial B}{\partial t} = k_i \frac{\partial T}{\partial y} - k_w \frac{\partial \theta}{\partial y} \tag{9}$$

In equations 6-9, θ and T are the temperatures, k_w and k_i are the thermal conductivities, C_{pw} and C_{pi} are the specific heats and h and B are the thicknesses of water and ice layers, respectively. On the other hand, ρ_i and L_F denote the density of ice and the latent heat of solidification of water, respectively. Ice density is assumed to have different values for rime ice, ρ_r and glaze ice, ρ_g. The coordinate y is normal to the surface and ρ_a is the liquid water content.

In equation (8), $\rho_a \beta V_\infty$, $\dot{m}_{in}$ and $\dot{m}_{e,s}$ are impinging, runback and evaporating (or sublimating) water mass flow rates for a control volume, respectively. The boundary and initial conditions accompanying equations (6-9) are [2]:

- Ice is in perfect contact with the wing surface:

$$T(0,t) = T_s \tag{11}$$

The surface temperature is taken to be the recovery temperature [3]:

$$T_s = T_a + \frac{V_\infty^2 - U_e^2}{2C_p}\frac{1+0.2rM^2}{1+0.2M^2} \tag{12}$$

In the above expression, $M = V_\infty/a_\infty$, while the speed of sound is given by $a_\infty = \sqrt{\gamma R T_a}$. Additionally, r is the adiabatic recovery factor.

- The temperature is continuous at the ice/water boundary and is equal to the freezing temperature, T_f :

$$T(B,t) = \theta(B,t) = T_f \tag{13}$$

- At the air/water (glaze ice) or air/ice (rime ice) interface, heat flux is determined by convection, radiation, latent heat release, cooling by incoming droplets, heat brought in by runback water, evaporation or sublimation, aerodynamic heating and kinetic energy of incoming droplets.

- Wing surface is initially clean:

$$B = h = 0, \;\; t = 0 \tag{14}$$

In the current approach, each panel constituting the geometry is also a control volume. The above equations are written for each panel and ice is assumed to grow perpendicularly to a panel.

Rime ice growth is expressed with an algebraic equation from the mass balance in equation (8), since water droplets freeze entirely on impact:

$$B(t) = (\rho_a \beta V_\infty / \rho_r)t \tag{15}$$

On the other hand, glaze ice thickness is obtained by integrating the ordinary differential equation obtained by combining mass and energy equations over time. The differential equation is:

$$\rho_g L_f \frac{\partial B}{\partial t} = \frac{k_i(T_f - T_s)}{B} + k_w \frac{(Q_c+Q_e+Q_d+Q_r)-(Q_a+Q_k)}{k_w + h^{(Q_c+Q_e+Q_d+Q_r)}/(T_s-T_a)} - Q_{ent} \tag{16}$$

In this expression, Q_c is heat flux by convection, Q_e is evaporation, Q_d is heat from incoming droplets, Q_r is radiation, Q_a is aerodynamic heating, Q_k is kinetic energy of incoming droplets and Q_{ent} is the energy entering the control volume due to runback water. It is assumed that, all of the unfrozen water passes to the neighboring downstream cell for the upper surface, while all water sheds for the lower surface[8]. To calculate the glaze ice thickness, equation (16) is integrated numerically, using a Runge-Kutta-Fehlberg method.

3. Results and Discussion

Ice shape predictions are obtained for NACA0012 airfoil geometry. The results are compared with the numerical data reported in the literature obtained with Lewice 2.0 and Lewice 3.0 (softwares developed by NASA) and experimental data which are presented by Wright and Potapzcuk [4]. Chord length of the airfoil is 0.53 m and the angle of attack is 0° for all the test cases. MVD, LWC, velocity, total temperature and exposure time are varying for the test cases which are shown in Table 1.

Table 1: Test cases for ice shape predictions

Test case	MVD (μm)	LWC (g/m^3)	Velocity (m/s)	T_{tot} (°C)	Exposure time (s)
Test 1-22	40	1.02	77	-19.3	576
Test 1-1	70	0.91	51	-19.6	804
Test 1-4	160	1.5	52	-19.5	300

In the calculations, multi-layer calculation approach and the effect of SLD are investigated. In multi-layer calculation approach, exposure time is divided into segments. At the beginning of each time interval, the iced surface is considered as the new geometry to be exposed to icing and all the calculations are repeated. The effect of SLD can be understood better by explaining the behavior of large droplets. Droplet breakup and splash are the phenomena which are characteristics of large droplets. Droplets with median volume diameter greater than about 100 μm are considered as SLD. Inclusion of SLD effects (breakup and splash) for the droplets with MVD lower than this value, does not

give correct results in the calculations. In the results, the cases for which the SLD effects are included are shown as "SLD: on". In the same manner, calculations performed without SLD effects are stated as "SLD: off".

Figure 1 and 2 show the parametric study of multi-layer calculation with and without the inclusion of SLD effects, respectively. The ice shapes obtained are compared with the experimental data. Although increasing number of layers does not change ice shape much, the result with 12 layers is slightly closer to the experimental data. The extent of ice and the ice shape in general is well-predicted, while there is a slight underestimation of the maximum ice thickness close to the leading edge. The ice shapes for this case are largely rime ice shapes due to low ambient temperature with relatively smooth contours but presence of horn-like shape suggests that there is also glaze ice present, due to high LWC and high speed, in spite of the low ambient temperature.

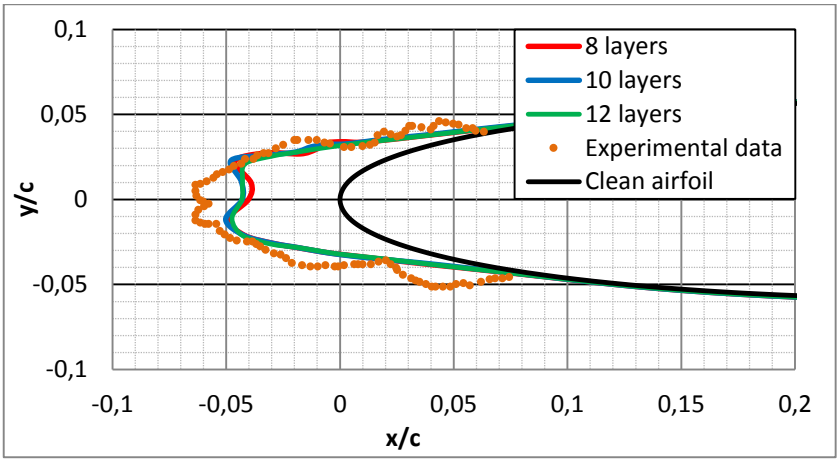

Figure 1: Ice shape predictions with different layers of calculation for Test 1-22 (SLD: on)

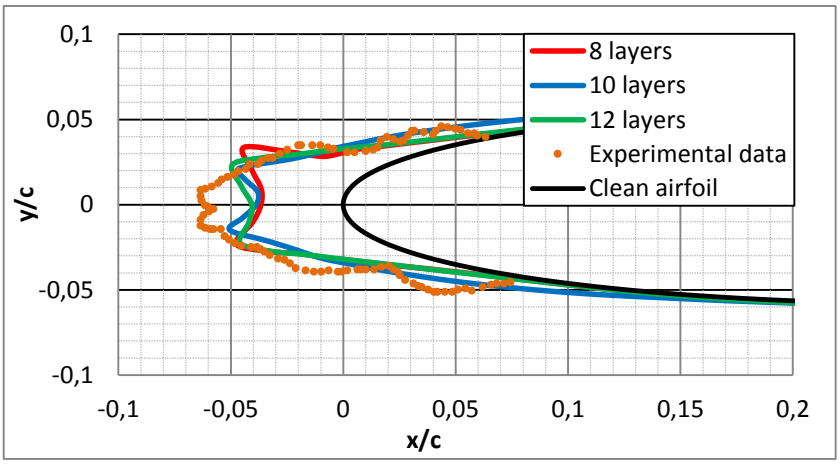

Figure 2: Ice shape predictions with different layers of calculation for Test 1-22 (SLD: off)

In Figure 3, the effect of SLD on ice shape prediction for 12 layers of calculation is shown. The prediction without SLD effect can be said to be better when compared with the experimental data in terms of symmetrical horn shape. This is expected since MVD for Test 1-22 is 40 µm which is not considered as SLD case and inclusion of breakup and splash does not improve the ice shape prediction.

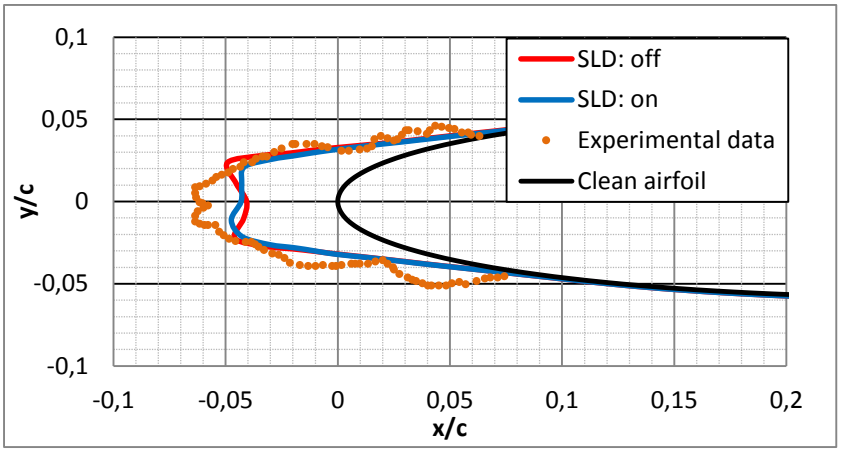

Figure 3: SLD effect on ice shape prediction for Test 1-22 (12 layers)

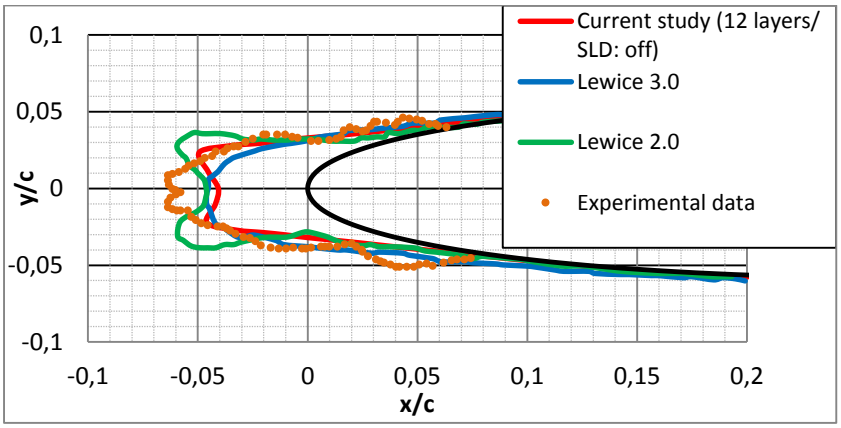

Figure 4: Comparison of current study result with reference numerical and experimental data for Test 1-22

The best ice shape prediction obtained is without SLD effects and 12 layers of calculation as shown above. This result is compared with numerical and experimental literature data in Figure 4. Although Lewice 2.0 predicts the horn shape well, it overestimates the ice thicknesses in the horn regions. Lewice 3.0 predicts a smaller ice mass and smoother ice shape. Current study captures the horn shape better than others, although it slightly underpredicts the ice thickness thinner than the experimental result.

In Figure 5 and 6, ice shape predictions for Test 1-1 are presented. As seen in both figures, increasing the number of calculation layers does not improve the results significantly, especially for the case where SLD effects are included. In Test 1-1, MVD=70 μm, which is not really an SLD case. This is backed up with Figure 7, which shows that a better ice shape is obtained by excluding droplet breakup and splash effects.

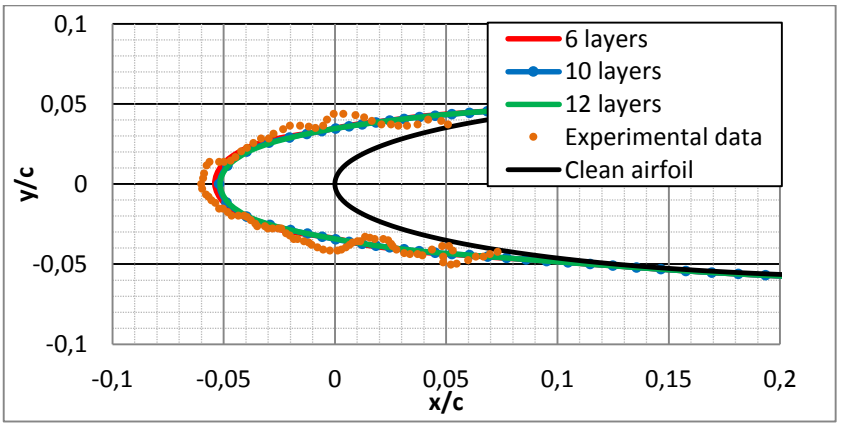

Figure 5: Ice shape predictions with different layers of calculation for Test 1-1 (SLD: on)

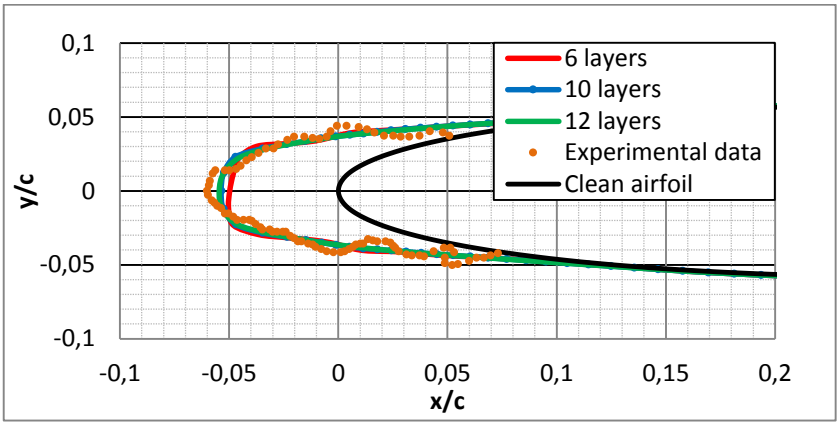

Figure 6: Ice shape predictions with different layers of calculation for Test 1-1 (SLD: off)

The ice shapes for this case suggest that the conditions are almost pure rime ice conditions due to low ambient temperature and speed, in spite of the not-so-low LWC.

Figure 8 shows the comparison of the results of the current study (12 layers of calculation, without SLD effects) with reference data. All the results can be said to be similar to each other when compared with the ice shape obtained in the experiment. The impingement zone is predicted slightly wider in both current and reference results. However, the current study is slightly better than the others in terms of ice thickness and the overall ice shape.

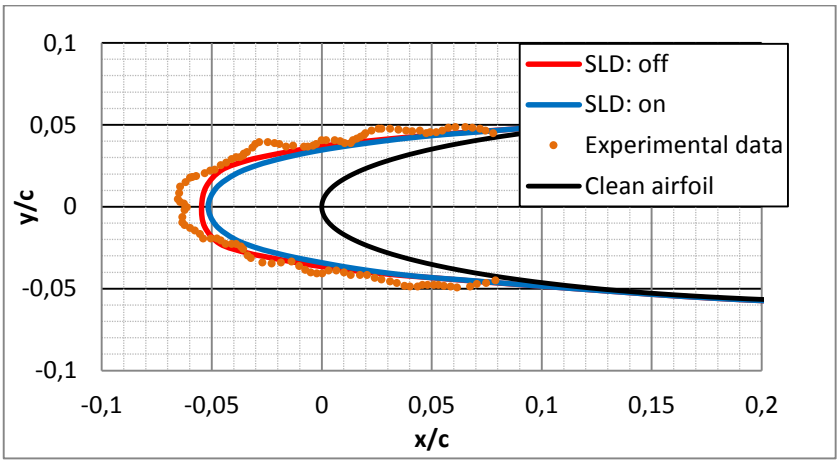

Figure 7: SLD effect on ice shape prediction for Test 1-1 (12 layers)

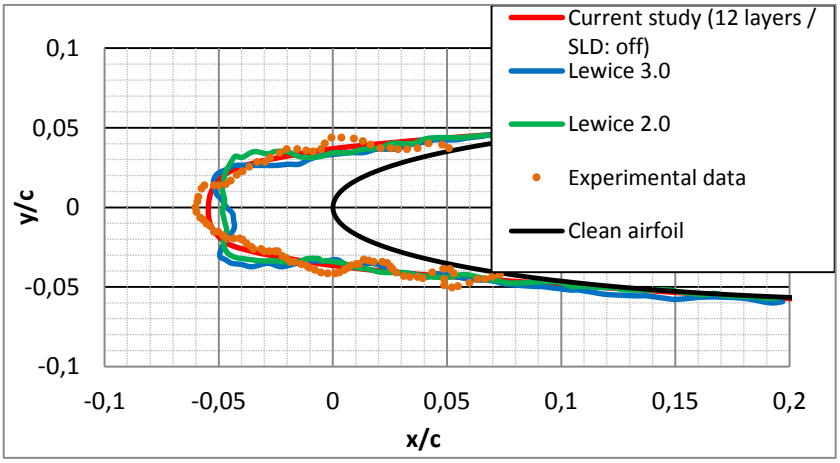

Figure 8: Comparison of current study result with reference numerical and experimental data for Test 1-1

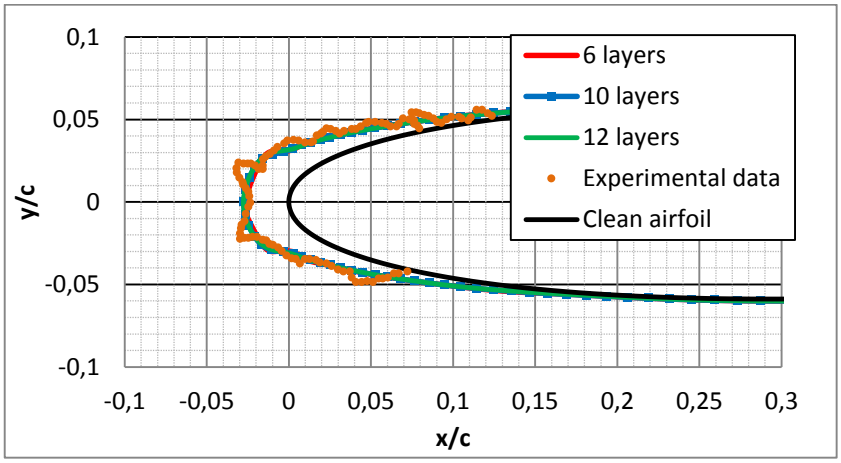

Figure 9: Ice shape predictions with different layers of calculation for Test 1-4 (SLD: on)

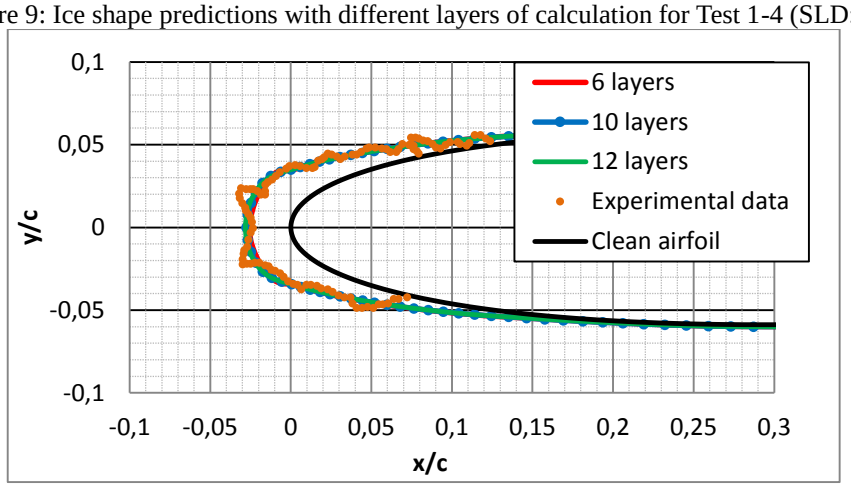

Figure 10: Ice shape predictions with different layers of calculation for Test 1-4 (SLD: off)

Droplet diameter is increased to 160 µm for Test 1-4. In Figure 9 and 10, it is clearly seen that increasing number of layers in the calculations does not improve ice shape prediction both for with and without SLD effects. This is mainly due to the fact that the ice shapes are almost pure-rime, where SLD effects play very little role as the droplets freeze immediately upon impact with the geometry. Moreover, Figure 11 shows that including SLD effects gives slightly closer ice shape prediction to experiment.

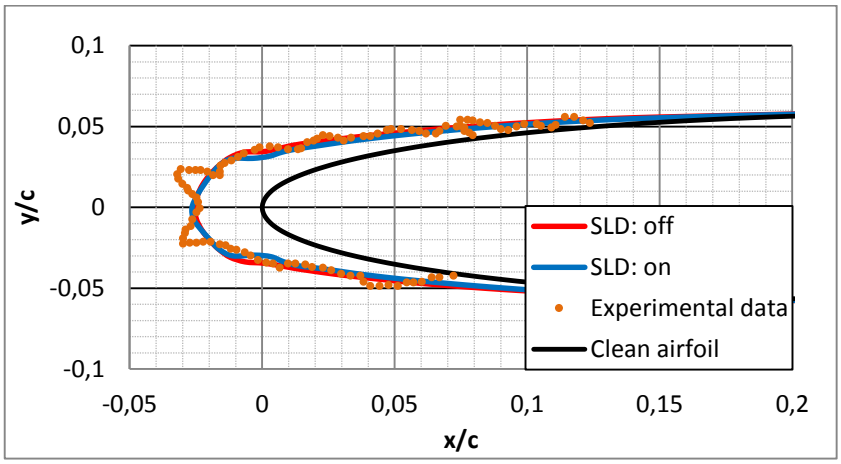

Figure 11: SLD effect on ice shape prediction for Test 1-4 (6 layers)

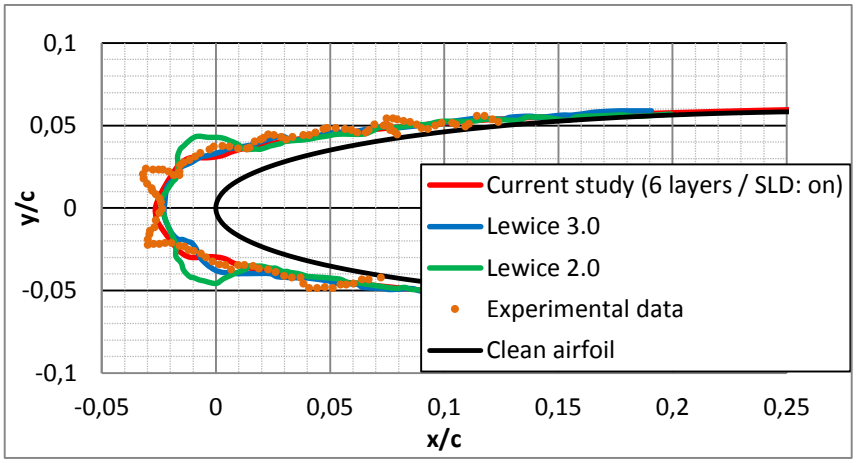

Figure 12: Comparison of current study result with reference numerical and experimental data for Test 1-4

For 6 layers of calculation and SLD: on case, current study result is shown with the numerical and experimental data in Figure 12. Lewice 2.0 obtains a thicker ice mass when compared with the others in the horn regions. Current study and Lewice 3.0 results are quite similar to each other which predict the thickness successfully, but miss the horn shapes.

In this part of the study, collection efficiencies are calculated for Twin Otter airfoil profile for varying droplet diameters and angles of attack. The validation study is performed for the flow over a profile with a chord length of 1.448 m and velocity of 78.25 m/s. Median droplet diameters vary between 11 µm to 168 µm. The analyses are done for $\alpha=0^o$ and $\alpha=4^o$. Collection efficiency results are validated with numerical and experimental data presented by Papadakis et al. [5]. Liquid water content sprayed out during the experiment varies with the droplet diameter which is as shown in Table 2. The droplets in the last two rows of the table are representative of SLD.

Table 2: LWC variation with MVD [5]

MVD (µm)	Average LWC (g/m^3)
11	0.188
21±0.5	0.521
79	0.496
137±2	0.680
168±3	0.747

Collection efficiency distributions for different droplet diameters are shown in the following figures. Horizontal axis shows the surface distance from highlight (mm) which is defined as in Figure 13 in [5]. It is clearly seen that highlight position is the leading edge of the airfoil. Negative values show the upper surface while positive values represent the lower surface.

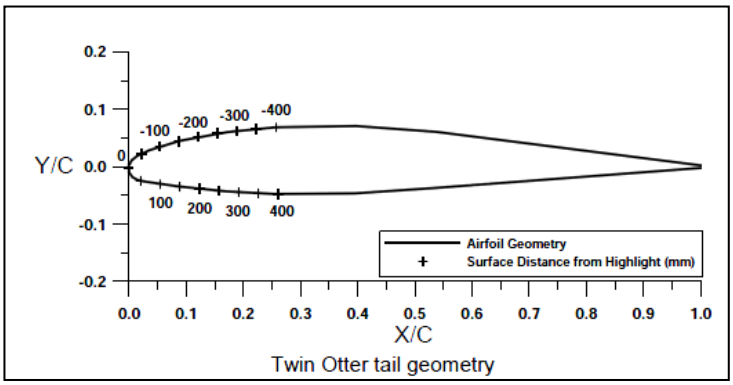

Figure 13: Definition of surface distance from highlight [5]

Figures 14, 15 and 16 show collection efficiency distributions for droplets with MVD of 11, 21, 79, 137 and 168 μm at α=0°. Current study results are compared with numerical results obtained with the software Lewice developed by NASA and also experimental data. Since the angle of attack is 0°, maximum collection efficiency value is at the leading edge where surface distance from highlight is 0 mm. The case corresponding to MVD=11 μm probably corresponds to the lower limit for the applicability of the drag coefficient formulations because the droplet Reynolds number is very small, which is probably a contributing factor to the discrepancy of the current results and the literature data. For the case MVD=21 μm, almost the same results are obtained from numerical and experimental literature data and the current study. Although the impingement zone is slightly underpredicted, the maximum β value is estimated well. When the other cases are investigated, it is seen that higher values of β are observed in the current study than the reference data, especially in the regions away from the leading edge. The same inference is also valid for Lewice results, especially to a higher extent for MVD=137 and 168 μm cases. From the Figures 14, 15 and 16, it can be deduced that collection efficiency distribution and maximum values are captured fairly successfully for α=0°.

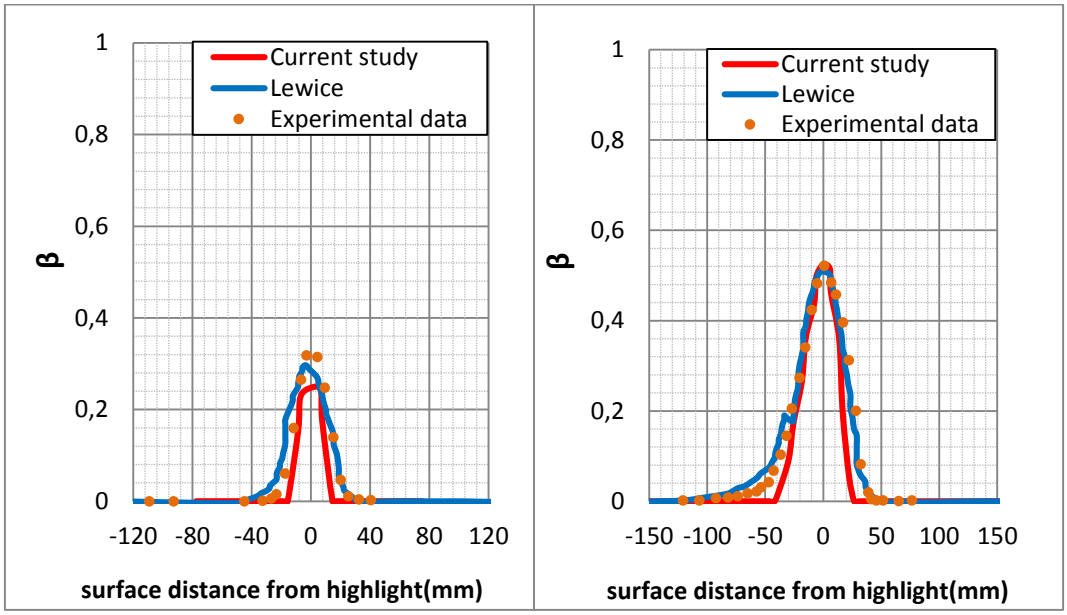

a. MVD=11 μm b. MVD=21 μm

Figure 14: Collection efficiencies for 11 μm and 21 μm (α=0°)

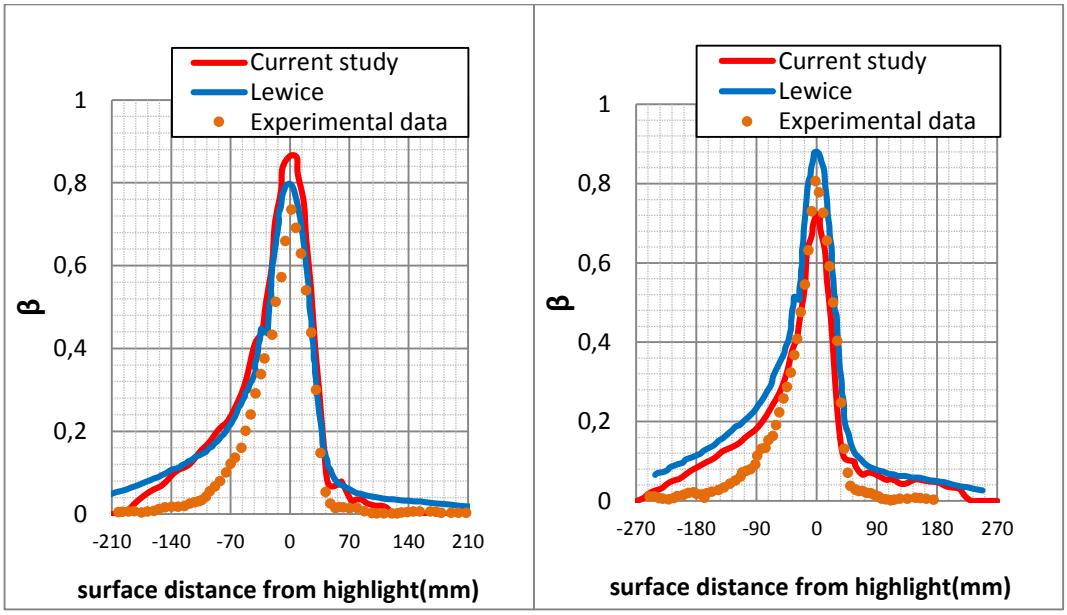

a. MVD=79 μm b. MVD=137 μm

Figure 15: Collection efficiencies for 79 μm and 137 μm (α=0°)

In Figure 17, collection efficiency distribution for varying droplet diameters is seen. As expected, increase in droplet diameter results in increase in β as well. Moreover, impingement limits both on lower and upper surface are wider for larger droplets. The reason for this is that, larger droplets have higher inertia and therefore follow ballistic trajectories. This results in more particles impinging the surface and the impingement angle being higher, resulting in higher collection efficiencies and wider impingement zones.

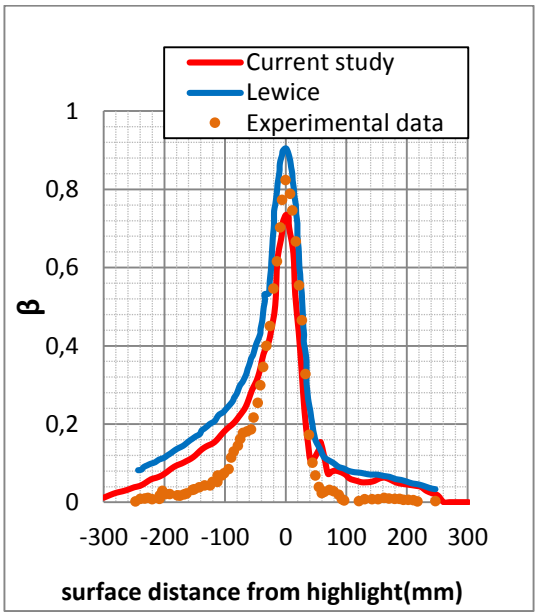

Figure 16: Collection efficiency for 168 µm (α=0°)

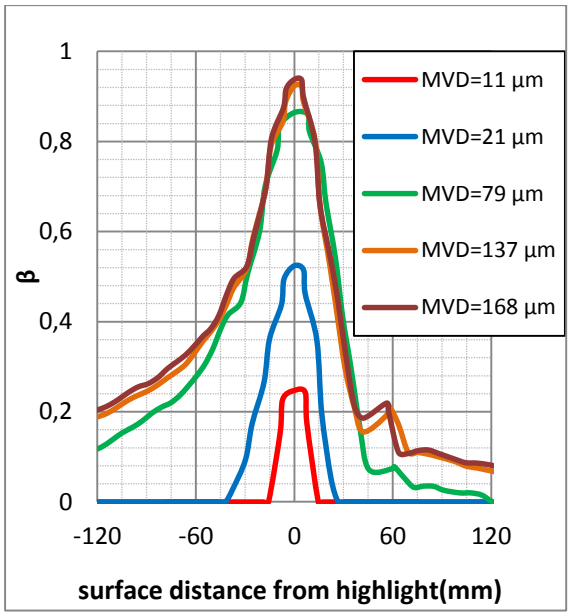

Figure 17: Collection efficiencies for varying MVD values (α=0°)

When angle of attack is increased to 4°, collection efficiency distributions are obtained as shown in Figures 18, 19 and 20. Due to angle of attack, maximum values of collection efficiency shift to right, in other words to the positions on the lower surface.

For α=4° cases, it is noticed that the maximum collection efficiency values are almost the same as for α=0° cases. Current study results where MVD=21 µm can be said to be the closest one to the experimental results. Similar results

to 0º cases are obtained for the other droplet diameter cases. The location of the maximum β value is predicted almost the same, although the maximum value itself is found different. As in 0º cases, impingement limits on lower and upper surfaces are calculated different as well. The current results indicate a slight overestimation of the collection efficiencies away from the leading edge especially for MVD=137 and 168 μm cases.

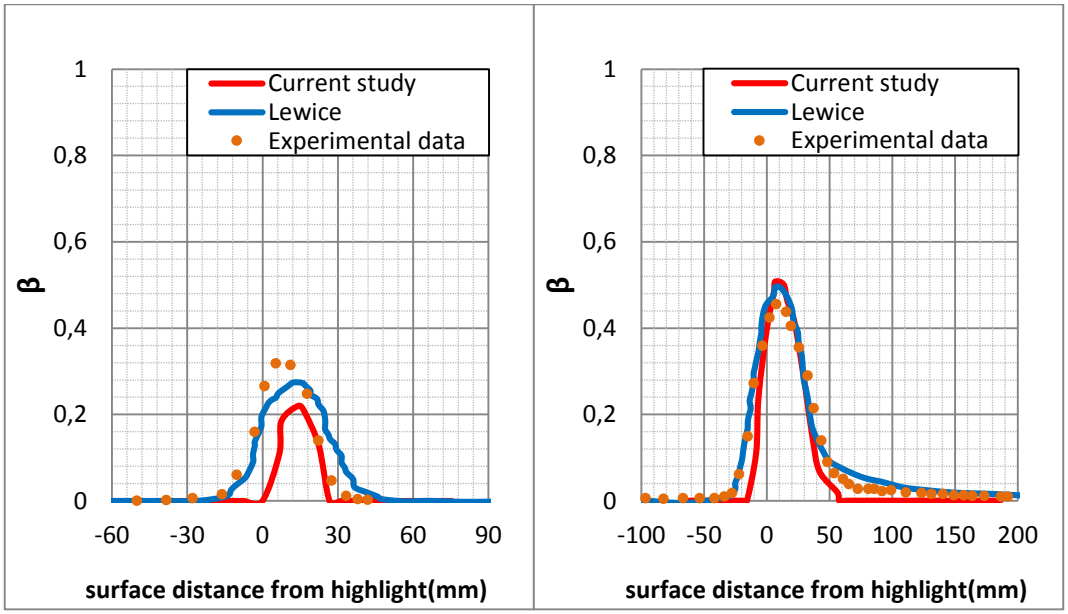

a. MVD=11 μm b. MVD=21 μm

Figure 18: Collection efficiencies for 11 μm and 21 μm (α=4º)

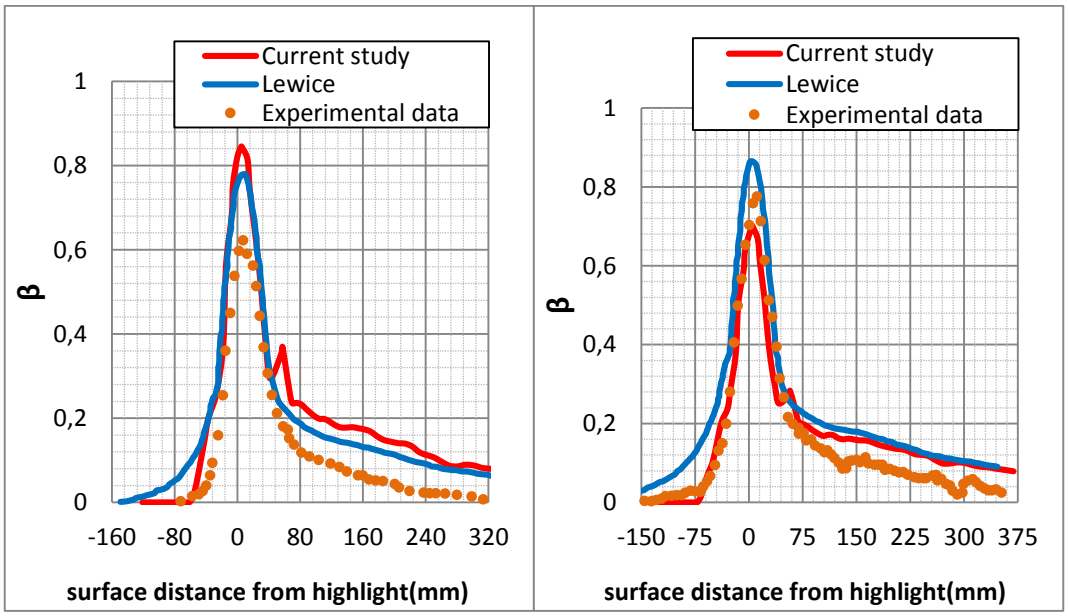

a. MVD=79 μm b. MVD=137 μm

Figure 19: Collection efficiencies for 79 μm and 137 μm (α=4º)

Figure 21 shows the collection efficiency for varying MVD values for angle of attack of 4º. Similar to 0º case, collection efficiency values are higher and impingement zone is wider for larger median volume diameter of droplets.

In this validation study, the effects of angle of attack and droplet diameter on collection efficiency are investigated. Maximum β values occur at the leading edge for zero angle of attack. When angle of attack is increased, ice accumulates more on lower surface and maximum value position shifts to here. For a given angle of attack,

increasing droplet diameter not only increases maximum β value, but also extends the impingement zone both on lower and upper surface.

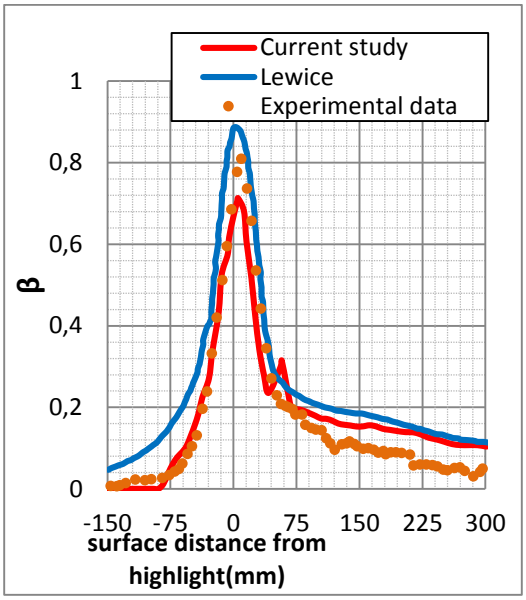

Figure 20: Collection efficiency for 168 µm (α=4°)

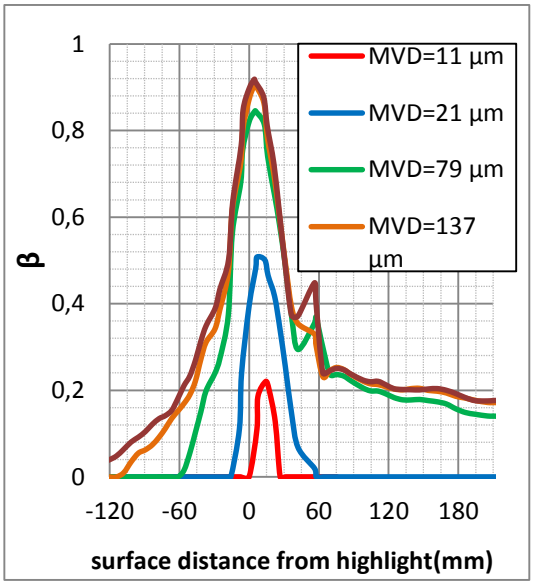

Figure 21: Collection efficiencies for varying MVD values (α=4°)

4. Conclusion

Ice shape predictions for NACA0012 airfoil geometry and collection efficiency calculations for Twin Otter airfoil geometry are performed in the current study. In the first validation study, it is seen that increasing number of layers of calculation improves ice shape prediction and a closer ice shape to experimental result is obtained. Moreover, for the droplets with median droplet diameter smaller than about 100 µm, including SLD effects like breakup and splash does not enhance the results unlike for the larger droplets. In the collection efficiency analysis, the effects of angle of attack and droplet diameter are studied. It is deduced that the maximum collection efficiency value occurs at the leading edge for zero angle of attack. Increase in angle of attack results in the shift of the position where maximum β value is observed, to the lower surface for positive angle of attack, although the value of this parameter itself seems to be fairly independent of angle of attack. Furthermore, for a given angle of attack, collection efficiency becomes higher and impingement zone widens when droplet diameter is increased. The results for both ice shape prediction

and collection efficiency show that current study results are in good agreement with the reference numerical and experimental data. It can be concluded that the current tool can be used for certification purposes as well as for the design of de/anti-icing equipment on aircraft.

References

[1] Özgen, S., and Canıbek, M., Ice accretion simulation on multi-element airfoils using extended Messinger model, *Heat and Mass Transfer*, Vol. 45 (3), pp. 305-322, 2009.

[2] Myers, T.G., Extension to the Messinger Model for aircraft icing, *AIAA J*., Vol. 39, pp. 211-218, 2001.

[3] Gent, R.W., Dart, N.P., and Cansdale, J.T., Aircraft Icing, *Phil. Trans. R. Soc. Lond. A*, Vol. 358, pp. 2873-2911, 2000.

[4] Wright, W.B., Potapczuk, M.G., Semi-empirical Modeling of SLD Physics, NASA TM-2004-212916, 2004.

[5] Papadakis M., Wong S., Rachman A., Hung K.E., Vu G.T., Bidwell C.S., Large and Small Droplet Impingement Data on Airfoils and Two Simulated Ice Shapes, NASA TM-2007-213959, 2007